

CrossMark
click for updatesCite this: *J. Mater. Chem. C*, 2015, 3, 2568

An n-type, new emerging luminescent polybenzodioxane polymer for application in solution-processed green emitting OLEDs†

Bipin Kumar Gupta,^{*a} Garima Kedawat,^b Pawan Kumar,^a Mohammad A. Rafiee,^c Priyanka Tyagi,^a Ritu Srivastava^a and Pulickel M. Ajayan^d

Herein, we report polybenzodioxane polymer (PIM-1), a multifunctional n-type emitter with strong green luminescence, and its suitability as an electron transport layer for OLEDs devices. The Brunauer–Emmett–Teller (BET) test and photo-electrical properties of as-synthesized PIM-1 confirm the presence of large microporosity and excellent electron mobility. The photoluminescence (PL) spectroscopy shows the intense green emission at 515 nm upon 332 nm excitation wavelength. Moreover, the Hall effect study reveals the negative Hall resistivity, which indicates that PIM-1 possesses n-type semiconductor characteristics. It enables the highly-efficient polymer-based green LEDs with configuration; ITO (120 nm)/PEDOT:PSS (30 nm)/PIM-1 (100 nm)/LiF (1 nm)/Al (150 nm), which are fabricated by the sequential solution-processing method. The OLED incorporating PIM-1 thin layer achieves maximum current efficiency of 1.71 Cd A⁻¹ and power efficiency of 0.49 lm W⁻¹. Additionally, the electron mobility is found to be 4.4 × 10⁻⁶ cm² V⁻¹ s⁻¹. Hence, these results demonstrate that PIM-1 could be an ultimate choice as an n-type emitter for the next generation of advanced electronic devices.

Received 12th November 2014
Accepted 12th January 2015

DOI: 10.1039/c4tc02581d

www.rsc.org/MaterialsC

1. Introduction

Organic light-emitting diodes (OLEDs) that use phosphorescent complexes as an emitting material have attracted considerable attention in the field of organic displays, owing to their potential use in high brightness flat-panel displays and solid state lighting device applications than OLEDs that use conventional fluorescent materials.^{1–3} Emissive materials effectively harvest and convert both singlet and triplet excitons into photons to obtain nearly 100% internal quantum efficiency^{4–6} and this greatly affects the electroluminescence properties, such as efficiency, driving voltage and lifetime. The potential for the use of OLEDs has led to a tremendous amount of research activity for the development of novel emissive materials and sophisticated device configurations. The efficiency of OLEDs is improved by incorporation of an electron-transport host material between the emissive layer and the cathode.^{7–10} In general, organic materials are p-type and have significantly higher mobility for holes in comparison to electrons, which leads to charge carrier

imbalance inside the emissive layers and more often, the exciton formation occurs at the emissive layer-electron transport layer interface. Emissive layers in OLED require a charge carrier balance for optimum efficiency and emissive materials with good electron mobilities are being developed for this purpose. In addition to mobility considerations, highest occupied molecular orbital (HOMO) (~5.5 eV) and high lying lowest unoccupied molecular orbital (LUMO) (~3.0 eV) are also required for efficient injection of holes and electrons from hole and electron transport layer, respectively into emissive layer. Several efforts have already been made for small molecular organic solar cells (OSCs) for developing efficient n-type emitters.^{11–13} However, polymers with such properties are still to be developed. There have been a few reports on electron transporting polymers with high field effect mobilities in the range of 10⁻³–10⁻⁵ cm² V⁻¹ s⁻¹, characterized using field effect transistors.¹⁴ However, field effect transistors operate at a very high electric field unlike the light emitting diodes, which work at rather low electric fields. Therefore, the polymers with multifunctional properties such as photoluminescence emission and electron transport for light emitting diode applications are highly desirable.

The most well-known strategies for the fabrication of OLEDs are thermal evaporation and solution processing methods. Although, the multilayered device structures fabricated by thermal deposition are widely used to balance charge transport and confine charge recombination,¹⁵ these have some drawbacks, such as expensive process and high manufacturing cost.¹⁶

^aCSIR-National Physical Laboratory, Dr K S Krishnan Road, New Delhi, 110012, India. E-mail: bipinbhu@yahoo.com; Fax: +91-11-45609310; Tel: +91-11-45609385

^bDepartment of Physics, University of Rajasthan, Jaipur, 302055, India

^cViva Technics Inc., 5 Thomas Mellon Circle, Suite 154, San Francisco, CA 94134, USA

^dDepartment of Mechanical Engineering and Materials Science, Rice University, 6100 Main Street, Houston, TX 77005, USA

† Electronic supplementary information (ESI) available. See DOI: 10.1039/c4tc02581d

In contrast, solution-processed OLEDs provide an economically better alternative to vacuum deposition due to their low cost and large-area manufacturability.^{17,18} However, fabrication of multi-layer layers is a challenging task due to the better match of orthogonal solvents that would not disrupt and dissolve the underlying layers. The emissive layer is fabricated by solution-processing while polymer-based OLEDs include thermally deposited electron and hole transport material layers and cathode interfacial layers or low work function cathodes. Thus, the development of facile synthesis using solution process with novel host materials is still an interesting part for the OLED applications. OLEDs based on solution processed layers containing few electron transport phosphorescent host materials exhibit highly efficient green phosphorescent emission.^{18–21}

A recent report on the synthesis of a polymer of intrinsic microporosity, polybenzodioxane-PIM-1 for gas sensing applications,^{22,23} could potentially lead to a major breakthrough due to its newly emerging luminescence properties as well as novel strategic application in organic light emitting diodes (OLEDs) devices as an n-type material. The polymer of intrinsic microporosity (PIM-1) is an insoluble, microporous and stable solid network. Soluble PIM-1 is precipitated to form a robust solid with large apparent surface area by nitrogen (N₂) adsorption. It is used for energy and environmental applications, including separation, adsorption and heterogeneous catalysis, owing to its exceptional high permeability, good selectivity and thermal and chemical stability of rigid and contorted macromolecular structures that cannot pack space efficiently.^{22,23} It also possesses excellent film forming properties, which can be used for the fabrication of devices by solution process.²⁴ The charge balance and electron injection from the cathode are important to realize highly efficient OLEDs. However, to the best of our knowledge, the use of luminescent PIM-1 material as an electron charge carrier in an effective polymer based OLEDs device has not been reported till date.

In this paper, we have attempted to convert a soluble precursor into an insoluble polymer powder by cross-linking. Thus, the dibenzodioxane formation reaction between monomer 3,3,3',3'-tetramethyl-1,1'-spirobisindane-5,5',6,6'-tetrol (A) and monomer 2,3,5,6-tetrafluorophthalonitrile (B) gave a nonnetwork polybenzodioxane (PIM-1), which is soluble in polar aprotic solvents such as tetrahydrofuran.²² The fluorescence microscopy of PIM-1 exhibits intense green emission peaking at 515 nm upon 332 nm excitation wavelength with higher quantum efficiency (~63%). This host thin layer of PIM-1 has to demonstrate good monopolar electron charge transport characteristics and charge trapping for the emitter. It also improves the efficiency of green luminescent OLED devices when PIM-1 thin layer of cross-linkable material is deposited by solution process between the multilayer devices as an electro-phosphorescent material. Thus, the solution-processed OLEDs exhibit the better performance to date in polymer-based green OLEDs. The approach of using solution-processed PIM-1 electron transport layer has resulted in high performance as green OLEDs with high luminous efficiency at 1.71 Cd A⁻¹. The PIM-1 layer shows a unique morphology, which facilitates luminescent, porosity, improved carrier mobility and higher device performance characteristics.

2. Experimental

2.1 Materials

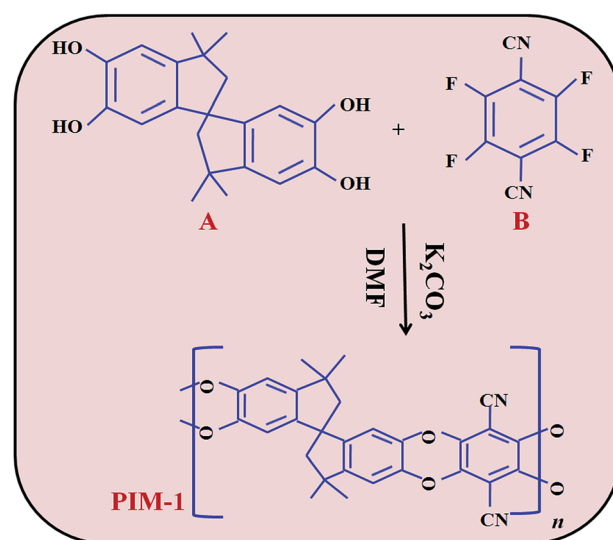
All the reagents and solvents used for the synthesis were purchased from Sigma Aldrich and were used without further purification.

2.2 Synthesis of PIM-1

The micro-porous PIM-1 was prepared with high yield (90%) by the polydioxane formation reaction between the corresponding difunctional monomers (A and B) as illustrated in Scheme 1. The chemical structures of the monomer and polymer are also shown in Fig. S1 (see ESI[†]). A mixture of monomer 3,3,3',3'-tetramethyl-1,1'-spirobisindane-5,5',6,6'-tetrol (5.12 g, 15.0 mmol), 2,3,5,6-tetrafluorophthalonitrile (3.01 g, 15.0 mmol) and anhydrous K₂CO₃ (0.70 g, 5.4 mmol) was stirred in dry dimethylformamide (100 ml) at 65 °C for 72 h.²² Upon cooling, the reaction mixture was added into de-ionized water (200 ml) and the solution was filtered. Then, the solid product was precipitated with methanol and collected, yielding 7.8 g (90% yields) of yellow fluorescent polymer. The polymer powder PIM-1 was dried in a vacuum oven prior to use (7.8 g, yield 90%). ¹H NMR (CDCl₃) 1.20–1.45 (12H, m), 2.09–2.46 (4H, m), 6.40 (2H, s), 6.82 (2H, s).

2.3 Characterizations

X-ray diffraction (XRD) measurements were carried out using a Rigaku Mini-flex Diffractometer, using Cu-Kα₁ radiation with a Ni filter (λ = 1.5406 Å at 30 kV and 15 mA). Raman spectra were recorded using Renishaw InVia Raman spectrometer, UK, with an excitation source of 514.5 nm. The surface morphology of PIM-1 was obtained by field emission scanning electron microscopy (FESEM, model no. EVO-MA 10 VPSEM). The

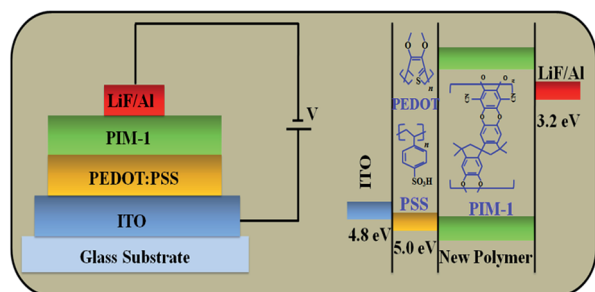


Scheme 1 Synthesis of PIM-1 polymer. A: 3,3,3',3'-tetramethyl-1,1'-spirobisindane-5,5',6,6'-tetrol, B: 2,3,5,6-tetrafluorophthalonitrile, DMF: dimethylformamide. A and B monomers and anhydrous K₂CO₃ were stirred in dry dimethylformamide at 65 °C for 72 h.

surface roughness was measured by atomic force microscopy (AFM) (model: NT-MDT Solver Scanning probe Microscope). UV-vis absorption spectrum was recorded on a Shimadzu spectrophotometer (UV-3600). The photoluminescence (PL) spectrum was recorded using luminescence spectrometer (Edinburgh, FLSP-900) with xenon flash lamp as source of excitation and time-resolved spectroscopy was performed using luminescence spectrometer (Edinburgh, FLSP-900) with EPL 375 nm picosecond pulsed diode laser as a source of excitation. In order to estimate the absolute luminescence quantum efficiency of PIM-1, we used an integrating sphere, which is equipped with Edinburgh spectrometer F-900 instrument. The estimation of quantum yield was based on the integrated fraction of luminous flux and radiant flux as per established standard method.²⁵ The PL mapping of PIM-1 films was performed by WITech alpha 300R+ Confocal PL microscope system (WITech GmBH, Ulm, Germany), where 375 nm diode laser was used as a source of excitation. The transport measurements were carried out using 14 T Physical Property Measurement System (PPMS) Quantum design. Nitrogen (N₂) adsorption-desorption measurements of PIM-1 at 77 K were carried out using a Micromeritics ASAP 2020 instrument. Prior to use, PIM-1 sample was degassed at 120 °C temperature for 16 hours under high vacuum.

2.4 Device fabrication and measurement

The device structure of OLEDs with the energy level diagram is shown in Scheme 2. ITO coated glass substrates (sheet resistance 20 Ohms per square) were ultrasonically cleaned with deionized water, acetone and isopropanol in sequence and then dried in a vacuum oven at 120 °C. For the current density-voltage (J - V) characteristics of PIM-1, it was spin coated on the cleaned ITO substrate from a chloroform solution with different thickness of 100, 120 and 140 nm at room temperature. The residual solvent was removed by annealing the samples in air at 100 °C for 1 hour. Then, the samples were transferred to the thermal evaporation chamber where LiF (1 nm)/Al (150 nm) cathode layer was deposited sequentially under a pressure of 4×10^{-6} Torr. Furthermore, the electroluminescence properties were studied using this polymer as an active layer with a device structure ITO (120 nm)/PEDOT:PSS (30 nm)/PIM-1 (100 nm)/LiF (1 nm)/Al (150 nm) in which additional poly(3,4-ethylenedioxythiophene):poly(styrenesulfonate) (PEDOT:PSS) layer was used



Scheme 2 Device structure of solution-processed OLEDs on ITO coated glass substrate with energy level diagram.

to improve the hole injection and it was annealed in air at 150 °C for 1 hour.

The current density-voltage-luminance (J - V - L) characteristics of the devices were measured using a Keithley 2400 sourcemeter interfaced with a luminance meter (LMT-1009). The electroluminescence (EL) spectrum was measured with a high resolution spectrometer (ocean optics HR-2000CG UV-NIR).

3. Results and discussion

XRD was performed to analyse the amorphous or crystalline nature of PIM-1. The XRD pattern of PIM-1 is shown in Fig. 1a and the inset shows the synthesized yellow powder PIM-1 sample under room light. The broad peak seen at $\sim 19.6^\circ$ is due to the surface characteristics of sample holder. The peak centered at $\sim 19^\circ$ indicates the amorphous characteristics of PIM-1. The Raman spectroscopy is a nondestructive tool for analyzing the degree of cure of polymers. The Raman spectra of monomers A and B are shown in the lower left and right part of Fig. 1b, respectively. The Raman spectrum of PIM-1 is also illustrated in upper part of Fig. 1b. The Raman spectrum of PIM-1 demonstrates that PIM-1 is fully formed and no other monomer groups remain after synthesis. The observed Raman bands are at 1300, 1400 and 2250 cm^{-1} . The SEM image of PIM-1 and its magnified view are shown in Fig. 1c and d, respectively, which shows a ball like (marked by a red circle in Fig. 1d) granular morphology and agglomerated with weak van der Waals forces. It is the main reason for the weak interaction of the particles in the matrix and confirms the porosity in the polymer.

The surface topology and morphogenesis of PIM-1 were examined by atomic force microscopy (AFM). The two dimensional (2D) and three dimensional (3D) AFM images of PIM-1

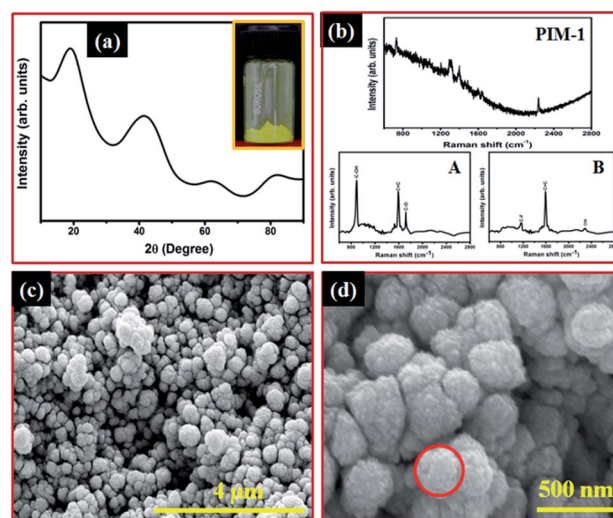


Fig. 1 (a) XRD spectrum of PIM-1; inset shows the synthesized yellow powder PIM-1 sample under room light, (b) Raman spectrum of polymer PIM-1 (upper part), monomer A (lower left part) and monomer B (lower right part), (c) SEM image of PIM-1 and (d) magnified SEM image view of (c).

are shown in Fig. 2a and b, respectively. Fig. 2a depicts the highly porous flake like structure of PIM-1, which is highlighted by a yellow colored boundary in Fig. S2 (see ESI†). The estimated surface roughness of PIM-1 film is $\sim 5 \pm 1$ nm, as seen in Fig. 2b. To demonstrate the porosity of the PIM-1 sample, the N_2 adsorption–desorption behavior at 77 K is shown in Fig. S3 (see ESI†). The obtained result exhibits a high sorption at very low relative pressure, which is the typical signature of a microporous polymer. The apparent surface area is calculated according to the (Brunauer–Emmett–Teller) BET method. The observed surface area is found to be ~ 683 m² g⁻¹. The relative low pressure portion of the adsorption isotherm is related to the apparent micropore distribution, which is calculated by the Horvath–Kawazoe method.²⁶ It reveals a significant proportion of micropores in the range 0.6–0.9 nm dimensions with mesopores coexisting to some content. Fig. S3† also exhibit a broad hysteresis and at low pressure, the hysteresis attributes to pore network effects.

The UV-vis absorption spectrum of PIM-1 is presented in Fig. 3a. It exhibits the absorption bands in the range of 280–550 nm. The intense peaks (232 and 296 nm) in the UV region below 400 nm are assigned to the allowed σ – π^* transitions and the weaker absorption tails that appear at about 444 nm to singlet and triplet transitions. The enhanced absorption in the solution-deposited PIM-1 polymer film suggests the formation of aggregates due to improved intermolecular interactions. Further, the luminescence property of PIM-1 has been explored by PL and time-resolved spectroscopy, which is a major focus of our present investigations. PL is a non-destructive direct optical tool to probe the electronic energy band structure and surface defect analysis. In present investigation, it can provide useful qualitative information about the interaction of de-localized electrons available at the surface of PIM-1 with oxygen induced defect states. The PL emission spectrum of the solution processed PIM-1 film at excitation wavelength 332 (3.7 eV) nm is shown in Fig. 3b and the inset exhibits the typical image of PIM-1 under room light as well as a 370 nm UV lamp (strong green emission appears). Under photo-excitation, a broad green emission spectrum with PL maximum peak centered at 515 nm (2.4 eV) is obtained with quantum yield ($\sim 63\%$), which is rarely reported in literature. This emission is designated as the transition of the π^* to π (lowest unoccupied molecular orbital

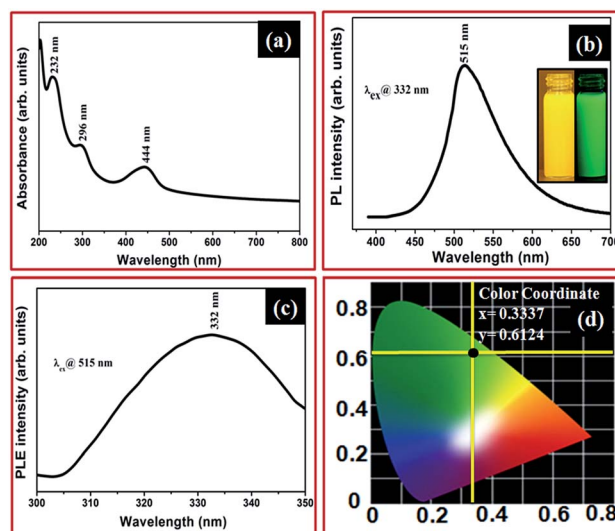


Fig. 3 (a) UV-vis absorbance spectrum of PIM-1, (b) PL emission spectrum of PIM-1 recorded at 332 nm excitation showing a strong green emission peak with maximum at 515 nm; inset exhibits the typical image of PIM-1 under room light as well as a 370 nm UV lamp (strong green emission appears), (c) PL excitation spectrum of PIM-1 at 515 nm emission wavelength and (d) CIE (chromaticity diagram) color coordinates of PIM-1, which is obtained from emission spectra are $x = 0.3337$ and $y = 0.6124$.

(LUMO) to highest occupied molecular orbital (HOMO)), as shown in the proposed energy level diagram for PIM-1 in Fig. S4 (see ESI†). The excitation spectrum of solution processed PIM-1 film at fixed emission wavelength of 515 nm is shown in Fig. 3c, which is recognized as a σ to π^* absorption. The CIE (chromaticity diagram) color coordinates of PIM-1, which is obtained from emission spectrum, are $x = 0.3337$ and $y = 0.6124$, as shown in Fig. 3d. The excitonic feature of PIM-1 structure represents the absorption energy corresponding to intense green emission light. The origin of luminescence can be explained in terms of existing de-localized π electrons on the surface of PIM-1 and its interaction with defects associated dangling bonds at the edge as well as at the surface of the PIM-1 structure. The major role of aromatic rings is to absorb efficient light and the energy transfer to available oxygen sites fluorophores. The CN functional group provides help to generate a more defective highly porous structure, leading to efficient ultraviolet light absorption in the host lattice. It is well known that the PIM-1 consists of oxidation chains with aromatic rings. This oxygen can absorb photons thereby generating oxygen vacancies under the ultraviolet excitation wavelength (332 nm), which is responsible for strong green PL emission of PIM-1. In other words, oxygen behaves like luminescence center for strong green emission. Thus, the strong PL is generated by the electron–hole recombination of available de-localized π electrons in the excited states (π^*) and their relaxation to ground state (π), whereas the excess excitation energy is trapped into the associated defects of PIM-1 structure.

The decay lifetime is an extremely important parameter to investigate the emission mechanism as well as for deciding the performance of materials for their suitable use. The efficiency of

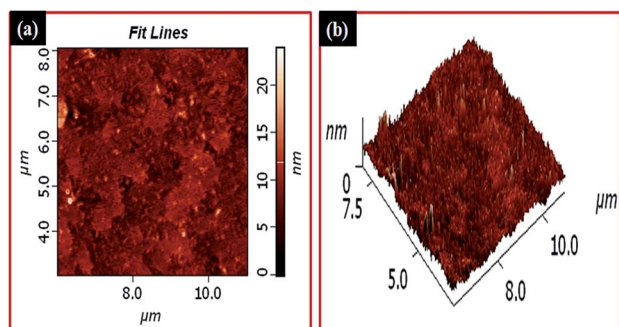


Fig. 2 (a) 2D AFM image of PIM-1 and (b) 3D AFM image of PIM-1.

radiative recombination is directly proportional to the decay time of the particular transition.²⁷ The decay spectrum was recorded for PIM-1 at 515 nm for green emission at room temperature by a time correlated single photon counting technique with a picosecond diode laser of 375 nm as a source of excitation. The lifetime data obtained from PIM-1 was best fitted to a double-exponential function as,

$$I(t) = A_1 \exp(-t/\tau_1) + A_2 \exp(-t/\tau_2) \quad (1)$$

where τ_1 and τ_2 are the decay lifetimes of the luminescence, and A_1 and A_2 are the weighing parameters. The lifetime data of green PIM-1 is shown in Fig. 4a and b. Fig. 4b demonstrates the exponential fitting of decay profile as described in eqn (1). The parameters generated from fitting are listed in the inset of Fig. 4b. The observed lifetimes are $\tau_1 \sim 4.61$ ns and $\tau_2 \sim 26.22$ ns. For double-exponential decay, the average lifetime, τ_{av} , is usually tailored to substitute the various components of the luminescence lifetime, which is determined by the following equation.^{27–30}

$$\tau_{av} = (A_1\tau_1^2 + A_2\tau_2^2)/(A_1\tau_1 + A_2\tau_2) \quad (2)$$

The average lifetime for PIM-1 is calculated as $\tau_{av} \sim 14$ ns. The presence of double exponential decay component indicates the presence of at least two electronically excited species. The coordination of aromatic rings with different ligand environments in PIM-1 could be the reason behind the observed double exponential decay. Therefore, the different components in the PL lifetime experiment provide experimental evidence that PIM-1 presents different coordination microenvironments, when excited under UV light. The obtained result is highly-suitable for proposed OLED device applications as well as many other optical display applications.

Prior to examining the hall resistivity, the PIM-1 film is deposited on a clean quartz substrate and the uniformity of PIM-1 film is determined using PL mapping measurement. Fig. 5a represents the optical image of PIM-1 film. Fig. 5b and c exhibit the 2D topological surface view and 3D lateral view of PIM-1. The PL mapping of PIM-1 (2D and 3D view) reveals that the PL intensity distribution is uniform throughout the film.

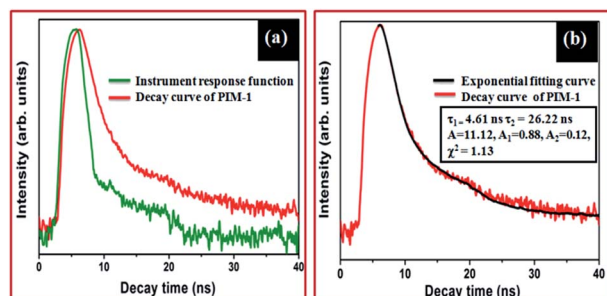


Fig. 4 (a) TRPL decay profile of PIM-1 recorded at room temperature with instrument response function and (b) decay profile of PIM-1 with exponential fitting and the inset shows the lifetime data and weighing parameters generated by the exponential fitting.

The PL mapping has been performed from the selected red marked square area in Fig. 5a. Further, Hall effect is used to determine the carrier concentration and sign of charge carriers in materials. It arises from the separation of charge carriers in the presence of an external magnetic field. The Hall resistivity (ρ_{xy}) is measured with longitudinal current and perpendicular magnetic field to the surface of the sample and the voltage (V_{xy}) is measured across the direction of the sample width. In Fig. 5d, the Hall resistivity of PIM-1 sample is plotted as a function of magnetic field at room temperature (300 K) and the inset shows the optical image of the prepared sample for Hall effect measurements. The Hall resistivity is found to be negative, which confirms the dominance of electronic charge carriers in the normal-state conduction mechanism. The strong nonlinearity of PIM-1 is observed with increasing magnetic field up to 1 Tesla, which is suggestive of deviations from single-band analysis. The charge carrier density at the magnetic field 1 Tesla is about $4.36 \times 10^{21} \text{ cm}^{-3}$. The Hall resistivity as a function of magnetic field at room temperature (300 K) of PIM-1 sample with error bar is also shown in Fig. S5 (see ESI†).

The electron transport of PIM-1 is investigated in ambient conditions by fabricating electron only devices with 100, 120 and 140 nm thickness. Measured J - V characteristics of the fabricated devices are shown in Fig. 6a. The current density of device (100 nm thick PIM-1 layer) is approximately two times higher than that of the 140 nm thick PIM-1 layer device. Hence, the current is solely due to electrons and the devices can be considered as electron only. At low applied bias voltages (below 3 V), the J - V characteristics show the ohmic conduction, which may be due to background impurity doping. As the voltage increases, a clear quadratic dependence of the current density on the voltage is readily observed, which indicates a trap free space charge limited conduction (SCLC) mechanism. The

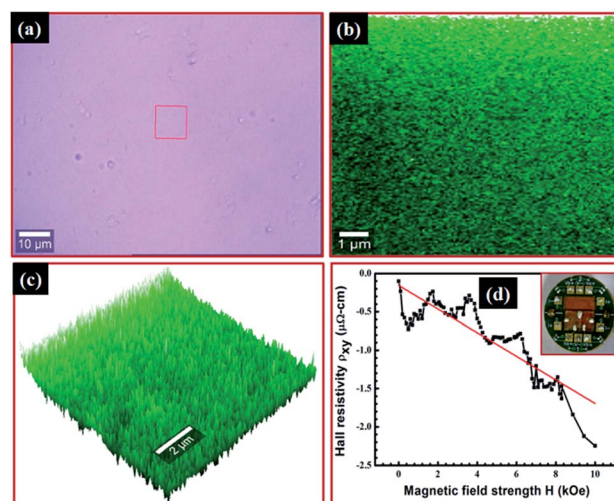


Fig. 5 (a) Optical image of PIM-1, (b) 2D view of PL mapping image of PIM-1 and (c) 3D lateral view of PL mapping image of PIM-1; the PL mapping has been performed from the selected red marked square area in (a) and (d) Hall resistivity as a function of magnetic field with linear fitting at room temperature and the inset shows the optical image of the prepared sample for Hall effect measurement.

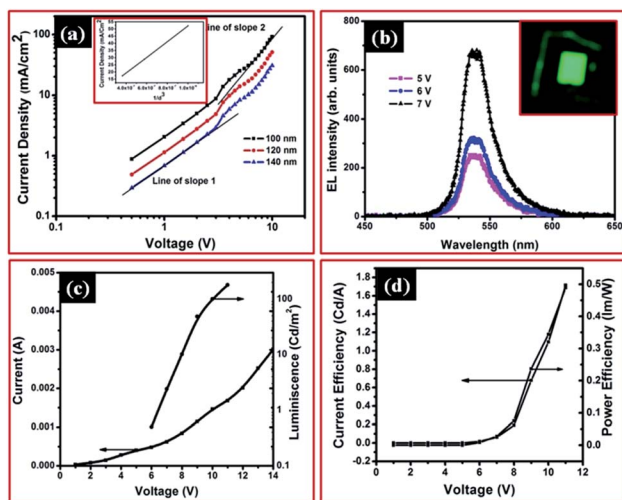


Fig. 6 (a) Current density–voltage characteristics, for varying the thickness (100, 120, 140 nm) of PIM-1; the inset shows the current density vs. $1/d^3$ curve, (b) EL spectra at different voltage (5, 6, and 7 V); the inset shows the optical image of fabricated green luminescence OLEDs device, (c) current–voltage–luminance characteristics for OLEDs with 100 nm thick electron transport PIM-1 layer and (d) current and power efficiency characteristics for OLEDs with 100 nm thick electron transport PIM-1 layer.

mobility can then be directly obtained from the J – V curve using Mott–Gurney's law, governing equation for trap free SCLC

$$J = \frac{9}{8} \mu \epsilon \frac{V^2}{l^3} \quad (3)$$

where ϵ , μ , V and l are the permittivity, mobility, applied voltage and active layer thickness, respectively. The solid lines in Fig. 6a represent the SCLC guiding curves in the quadratic J – V region. At higher voltages, the current density is found from eqn (3), which could be ascribed to the field and charge carrier density dependence of mobility. Electron mobility is evaluated in a voltage range 3–7 V (~ 3 – 7×10^5 V cm $^{-1}$ electric field), found to be 4.4×10^{-6} cm 2 V $^{-1}$ s $^{-1}$ and reaches a value of 10^{-5} cm 2 V $^{-1}$ s $^{-1}$ at electric fields of 10^6 V cm $^{-1}$. The values are found comparable to the reported values measured using time of flight methods for other polymers based on polyfluorene³¹ and phenylquinoxaline.³² However, the later reports are on very thick polymers (~ 4 μ m) and are not directly applicable in the case of OLEDs. Our reports are directly applicable here because of relatively low thickness (~ 100 nm) of OLEDs. The high electron mobility of PIM-1 makes it an ideal candidate for optoelectronic devices because the choice of n-type polymers with good thermal stability is rather limited. The thickness dependence on current density is also required in order to confirm the SCLC mechanism in devices.

Fig. 6a also shows the J – V characteristics of the electron only devices for different thicknesses of PIM-1. The current density depends on the thickness and maximum current densities are 91.43, 50.79 and 30.97 mA cm $^{-2}$ for 100, 120 and 140 nm thick devices, respectively. The current density is also found to scale with $1/d^3$, which confirms the occurrence of SCLC in the devices, as shown in the inset of Fig. 6a. This higher achieved

mobility is the significance of PIM-1 because it is quite difficult to obtain trap free SCLC in polymers for electron transport. Trap states reduce the electron current and trap free SCLC is achieved without any extra effort in this study. The higher electron mobility is due to the excellent solid state morphology of PIM-1, which enables the relative ease of electron injection and transport from PIM-1/Al interface. The EL properties of fabricated electroluminescent device with structure ITO (120 nm)/PEDOT:PSS (30 nm)/PIM-1 (100 nm)/LiF (1 nm)/Al (150 nm) are also monitored. Fig. 6b depicts the EL spectra of the device at different voltages showing green emission from PIM-1 centered at wavelength 535 nm. The inset of Fig. 6b shows the optical image of device with intense green emission at applied 7 V dc power supply. The optical images of fabricated OLEDs devices before and after the applied 7 V dc power supply are also shown in Fig. S6 (see ESI†). Fig. 6c shows the current–voltage–luminance (I – V – L) characteristics of the fabricated EL device, demonstrating good performance over a wide range of current densities. Further, we have also calculated current and power efficiency of the devices, which is depicted in Fig. 6d. An incremental pattern of efficiency with voltage is observed. The maximum current and power efficiencies are found to be 1.71 Cd A $^{-1}$ and 0.49 lm W $^{-1}$ at 11 V, respectively. This clearly demonstrates that the solution processed PIM-1, as an n-type emitter, efficiently confines charge carriers and excitons within the emission layer. Therefore, we conclude that the designed PIM-1 polymer is an excellent n-type emitter for optoelectronic applications as OLEDs. The charge conduction in this polymer is due to trapping free SCLC, which increases its significance as an n-type material.

4. Conclusions

In summary, we have successfully demonstrated a multifunctional n-type PIM-1 emitter with strong green luminescence of PIM-1 and its suitability as an electron transport layer for OLEDs devices. The surface morphology, BET result and photoelectrical properties of as-synthesized PIM-1 prove the presence of large microporosity and excellent electron mobility. Furthermore, the Hall effect study confirms the PIM-1 possessing n-type semiconductor characteristics. The fabricated OLED device based on PIM-1 material has achieved maximum current efficiency of 1.71 Cd A $^{-1}$ and power efficiency of 0.49 lm W $^{-1}$. Additionally, electron mobility is found to be 4.4×10^{-6} cm 2 V $^{-1}$ s $^{-1}$, significantly higher than other well established n-type polymers used for OLED devices. Hence, these results clearly show that PIM-1 is a very efficient polymer for use as an electron transport layer in the design of solution-processed OLEDs, with high electron mobility and low-lying LUMO energy levels for next-generation flat panel displays and solid state lighting applications.

Acknowledgements

One of the authors, Dr Bipin Kumar Gupta, is thankful for financial support from Indo-US Science and Technology Forum, New Delhi, India (IUSSTF): Award no. Indo-US Research

Fellowship/2010–2011/25-2010. The authors wish to thank Prof. R. C. Budhani, Director, N.P.L., New Delhi for his keen interest in the work. The authors are thankful to Prof. O. N. Srivastava (Banaras Hindu University, Varanasi) for his encouragement. The authors gratefully acknowledged University Grant Commission (UGC) and Council of Scientific and Industrial Research (CSIR), Govt. of India for financial assistance to carry out this work. The authors thank Dr V. P. S. Awana for Hall effect measurement of PIM-1 polymer. The authors are grateful to the CSIR-TAPSUN program providing PL mapping facility.

References

- M. A. Baldo, D. F. O'Brien, Y. You, A. Shoustikov, S. Sibley, M. E. Thompson and S. R. Forrest, *Nature*, 1998, **395**, 151–154.
- S. Reineke, F. Lindner, G. Schwartz, N. Seidler, K. Walzer, B. Lussem and K. Leo, *Nature*, 2009, **459**, 234–238.
- C. Adachi, M. A. Baldo, M. E. Thompson and S. R. Forrest, *J. Appl. Phys.*, 2001, **90**, 5048–5051.
- L. Xiao, Z. Chen, B. Qu, J. Luo, S. Kong, Q. Gong and J. Kido, *Adv. Mater.*, 2011, **23**, 926–952.
- F. M. Hsu, C. H. Chien, P. I. Shih and C. F. Shu, *Chem. Mater.*, 2009, **21**, 1017–1022.
- T. Earmme, E. Ahmed and S. A. Jenekhe, *J. Phys. Chem. C*, 2009, **113**, 18448–18450.
- S. J. Su, Y. Takahashi, T. Chiba, T. Takeda and J. Kido, *Adv. Funct. Mater.*, 2009, **19**, 1260–1267.
- Y. J. Li, H. Sasabe, S. J. Su, D. Tanaka, Y. J. Pu and J. Kido, *Chem. Lett.*, 2010, **39**, 140–141.
- H. Sasabe, D. Tanaka, D. Yokoyama, T. Chiba, Y. J. Pu, K. I. Nakayama, M. Yokoyama and J. Kido, *Adv. Funct. Mater.*, 2011, **21**, 336–342.
- D. F. O'Brien, M. A. Baldo, M. E. Thompson and S. R. Forrest, *Appl. Phys. Lett.*, 1999, **74**, 442–444.
- M. Ichikawa, S. Mochizuki, H. G. Jeon, S. Hayashi, N. Yokoyama and Y. Taniguchi, *J. Mater. Chem.*, 2011, **21**, 11791–11799.
- W. White, Z. M. Hudson, X. Feng, S. Han, Z. H. Lu and S. Wang, *Dalton Trans.*, 2010, **39**, 892–899.
- C. Wang, L. O. Palsson, A. S. Batsanov and M. R. Bryce, *J. Am. Chem. Soc.*, 2006, **128**, 3789–3799.
- X. Zhaoab and X. Zhan, *Chem. Soc. Rev.*, 2011, **40**, 3728–3743.
- J. Chen, C. Shi, Q. Fu, F. Zhao, Y. Hu, Y. Feng and D. Ma, *J. Mater. Chem.*, 2012, **22**, 5164–5170.
- X. H. Yang, D. C. Muller, D. Neher and K. Meerholz, *Adv. Mater.*, 2006, **18**, 948–954.
- C. L. Lee, K. B. Lee and J. J. Kim, *Appl. Phys. Lett.*, 2000, **77**, 2280–2282.
- H. Huang, Y. Wang, S. Zhuang, X. Yang, L. Wang and C. Yang, *J. Phys. Chem. C*, 2012, **116**, 19458–19466.
- A. Haldi, B. Domercq, B. Kippelen, R. D. Hreha and J. Y. Cho, *Appl. Phys. Lett.*, 2008, **92**, 253502.
- E. Y. Choi, J. H. Seo, H. M. Kim, K. H. Lee, H. J. Kang, S. S. Yoon and Y. K. Kim, *Jpn. J. Appl. Phys.*, 2010, **50**, 01BC07.
- S. J. Yoo, H. J. Yun, I. Kang, K. Thangaraju, S. K. Kwon and Y. H. Kim, *J. Mater. Chem. C*, 2013, **1**, 2217–2223.
- P. M. Budd, E. S. Elabas, B. S. Ghanem, S. Makhseed, N. B. McKeown, K. J. Msayib, C. E. Tattershall and D. Wang, *Adv. Mater.*, 2004, **16**, 456–459.
- B. S. Ghanem, N. B. McKeown, P. M. Budd, J. D. Selbie and D. Fritsch, *Adv. Mater.*, 2008, **20**, 2766–2771.
- Q. Song, S. Cao, P. Zavala-Rivera, L. P. Lu, W. Li, Y. Ji, S. A. Al-Muhtaseb, A. K. Cheetham and E. Sivaniah, *Nat. Commun.*, 2013, **4**, 1–9.
- K. Mishra, S. K. Singh, A. K. Singh, M. Rai, B. K. Gupta and S. B. Rai, *Inorg. Chem.*, 2014, **53**, 9561–9569.
- G. Horvath and K. Kawazoe, *J. Chem. Eng. Jpn.*, 1983, **16**, 470–475.
- B. K. Gupta, P. Thanikaivelan, T. N. Narayanan, L. Song, W. Gao, T. Hayashi, A. L. M. Reddy, A. Saha, V. Shanker, M. Endo, A. A. Marti and P. M. Ajayan, *Nano Lett.*, 2011, **11**, 5227–5233.
- S. Murakami, M. Herren, D. Rau and M. Morita, *Inorg. Chim. Acta*, 2000, **300–302**, 1014–1021.
- T. Fujii, K. Kodaira, O. Kawauchi and N. Tanaka, *J. Phys. Chem. B*, 1997, **101**, 10631–10637.
- B. K. Gupta, V. Rathee, T. N. Narayanan, P. Thanikaivelan, A. Saha, Govind, S. P. Singh, V. Shanker, A. A. Marti and P. M. Ajayan, *Small*, 2011, **7**, 1767–1773.
- A. J. Campbell, D. D. C. Bradley and H. Antoniadis, *Appl. Phys. Lett.*, 2001, **79**, 2133–2135.
- M. Redecker, D. D. C. Bradley, M. Jandke and P. Strohriegel, *Appl. Phys. Lett.*, 1999, **75**, 109–111.